

Geometric frustration and Dzyaloshinskii-Moriya interactions in a quantum star lattice hybrid copper sulfate

Hajime Ishikawa ^{*}, Yuto Ishii, Takeshi Yajima , Yasuhiro H. Matsuda, and Koichi Kindo
Institute for Solid State Physics, University of Tokyo, Kashiwa, Chiba 277-8581, Japan

Yusei Shimizu 
Institute for Materials Research, Tohoku University, Oarai, Ibaraki 311-1313, Japan

Ioannis Rousochatzakis 
Department of Physics, Loughborough University, Loughborough LE11 3TU, United Kingdom

Ulrich K. Röbller and Oleg Janson [†]
Institute for Theoretical Solid State Physics, Leibniz IFW Dresden, 01069 Dresden, Germany

 (Received 29 December 2022; revised 4 April 2024; accepted 5 April 2024; published 2 May 2024)

We study the magnetism of a layered, spin- $\frac{1}{2}$ organic-inorganic copper sulfate, which is a close realization of the star lattice antiferromagnet, one of the playgrounds of geometric frustration and resonating valence bond physics in two spatial dimensions. Our thermodynamic measurements show no ordering down to 0.1 K and a characteristic field-induced entropic shift, revealing the presence of an infinite number of competing states down to very-low-energy scales. The response to external magnetic fields shows, in addition, a peculiar anisotropy, reflected in the formation of a $1/3$ magnetization plateau (stable up to full saturation around 105 T) and a paramagnetic, Curie-like susceptibility for one direction of the field ($\mathbf{H} \parallel \mathbf{c}$), and a completely different response in other field directions. Our first-principles density functional theory calculations and exact diagonalizations show that these experimental puzzles are distinctive signatures of a strong interplay between geometric frustration and sizable Dzyaloshinskii-Moriya interactions, and the emergence of a continuous $U(1)$ symmetry at low-energy scales.

DOI: [10.1103/PhysRevB.109.L180401](https://doi.org/10.1103/PhysRevB.109.L180401)

Introduction. The problem of tiling a plane with regular convex polygons has fascinated architects since ancient times, engendering a rich cross-cultural heritage. In modern condensed-matter physics, the very same patterns appear in a different context: antiferromagnetically coupled localized spins arranged on the vertices of a tiling are at the heart of frustrated magnetism [1,2] and high-temperature superconductivity [3]. The emergent spin lattices split into two classes. Bipartite lattices, such as the square or the honeycomb lattice, feature the classical Néel ground state (GS), which is globally compatible with all antiferromagnetic (AFM) bonds. Such compatibility is fundamentally impossible in geometrically frustrated lattices, where only local constraints can be satisfied. For instance, in the kagome lattice [Fig. 1(a)], the local constraint imposes a 120° -spin structure within each triangle. Since infinitely many *global* configurations satisfy this *local* constraint, the classical GS manifold is infinitely degenerate. In the case of spin- $\frac{1}{2}$, quantum fluctuations may stabilize exotic GSs such as quantum spin liquids [4–6] and valence bond phases [7–9].

The spin- $\frac{1}{2}$ star lattice antiferromagnet [Fig. 1(a)] is one of the paradigmatic models of geometrically frustrated magnetism in two spatial dimensions [1,2,10]. As in the kagome lattice, the triangle-based structure leads to an infinite ground-state degeneracy at the classical level [11] and an array of unconventional GSs in the spin $S = 1/2$ limit, including valence bond solids [11–13], resonating valence bond states [14], chiral spin liquids [15], and magnetic field-induced phase transitions [11,13]. Unlike the kagome lattice, the star lattice features two inequivalent nearest-neighbor (NN) bonds. The respective Heisenberg exchange interactions are often called J_T and J_D , as the spins on these bonds are part of a triangle and a dimer, respectively. The lattice can also be viewed as a (decorated) honeycomb lattice made of triangles.

Layered sulfates often provide peculiar spin lattices such as kagome lattice in natural minerals [16,17] and organic-inorganic materials [18,19]. In 2020, Sorolla *et al.* reported $[(\text{CH}_3)_2(\text{NH}_2)]_3\text{Cu}_3(\text{OH})(\text{SO}_4)_4 \cdot 0.24\text{H}_2\text{O}$, (dimethylammonium copper sulfate, called DiMACuS hereafter), which is the first realization of the spin- $\frac{1}{2}$ star lattice made of Cu^{2+} ($3d^9$) ions [20]. The crystal structure features inorganic $[\text{Cu}_3(\text{OH})(\text{SO}_4)_4]^{3-}$ layers separated by dimethylammonium cations and crystal water molecules. In addition to J_T and J_D , the next-nearest-neighbor interaction,

^{*}hishikawa@issp.u-tokyo.ac.jp

[†]o.janson@ifw-dresden.de

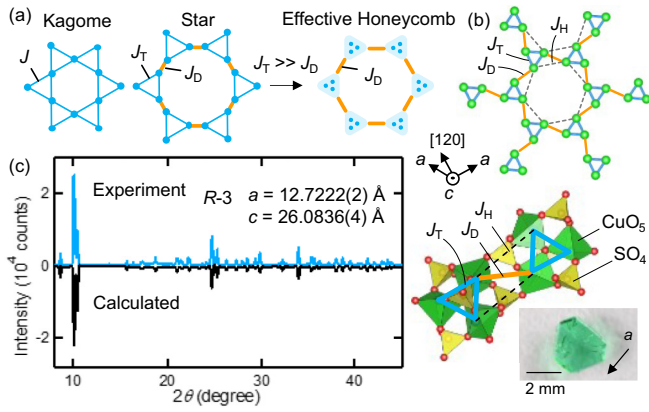


FIG. 1. (a) Kagome and star lattices. Close to the isolated-triangle limit ($J_T \gg J_D$), the star lattice can be described as a honeycomb lattice made of spin triangles. (b) Isotropic exchange interactions in DiMACuS (top): the (a, b, c) frame shown refers to the hexagonal unit cell. Local crystal structure (bottom) described by CuO_5 pyramid and SO_4 tetrahedra, as plotted using VESTA [22]. A picture of a single crystal is also shown. (c) Observed and calculated powder x-ray diffraction patterns.

called J_H here [Fig. 1(b)], which forms the hexagon, may be present due to the rotation of the triangles. Similarly modified next-nearest-neighbor interactions are found in a classical kagome AFM and their effect on the GS has been examined previously [21]. Sorolla *et al.* observed paramagnetic behavior down to 1.8 K in spite of an AFM Weiss temperature of 41 K and proposed DiMACuS as a quantum spin liquid candidate [20].

In this Letter, we report the successful synthesis of millimeter-size single crystals of DiMACuS as well as pure powder suitable for detailed magnetic characterizations. We performed magnetization measurements on single crystals down to 0.1 K and measured the entire magnetization process of the powder sample in pulsed magnetic fields up to 120 T. We also measured the specific heat with and without magnetic fields. Two remarkable experimental results are the absence of magnetic ordering down to 0.1 K and a peculiar magnetization anisotropy, with a 1/3 plateau visible only in $\mathbf{H} \parallel \mathbf{c}$. By combining first-principles calculations with analytical and numerical model simulations, we show that DiMACuS is a quantum star lattice magnet with $J_T \gg J_D$ and substantial chiral Dzyaloshinskii-Moriya (DM) interactions within the spin triangles.

Synthesis. The sample was prepared by reacting 0.4 g of $\text{CuSO}_4 \cdot 5\text{H}_2\text{O}$, 0.5 ml of sulfuric acid and 5 ml of *N,N*-dimethylformamide in a glass vial at 80 °C for a few days. An aggregation of bright green crystals including hexagonal plates of a few millimeter size is formed [Fig. 1(b)]. The aggregation is recovered by decantation and washed by *N,N*-dimethylformamide. The sample is immediately vacuum dried and stored inside an argon-filled glove box as the crystal is hygroscopic. The crystal is covered by Apiezon-N grease or sealed inside a plastic tube before being exposed to air for measurements. Powder x-ray diffraction measurement is performed on the crushed crystals by a diffractometer with $\text{Cu-K}\alpha_1$ radiation (Smart Lab, Rigaku). The observed pattern

matches well with the calculated pattern of DiMACuS with the space group $R\bar{3}$ and lattice constants $a = 12.7222(2)$ and $c = 26.0836(4)$ Å, indicating the successful synthesis: the pattern calculation is performed by FULLPROF software [23] including the effect of preferred orientation along the c axis.

Low-field magnetization measurements. The magnetization of a single crystal was measured by a SQUID magnetometer (MPMS-XL, Quantum Design) in the T range 1.8–300 K and magnetic fields of up to 5 T. We made a Curie-Weiss fit to the magnetic susceptibility χ using the expression $\chi(T) = \chi_0 + C/(T + \Theta)$, where C and Θ are the Curie constant and the Weiss temperature, respectively, and χ_0 is the T -independent term. Above 150 K, we obtain $C = 0.469(8)$ emu/mol Cu K ($\mu_{\text{eff}} = 1.94 \mu_B$), $\Theta = 43(2)$ K, and $\chi_0 = -3.0(1) \times 10^{-4}$ emu/mol Cu for $\mathbf{H} \parallel \mathbf{c}$. The same fit for the data in $\mathbf{H} \parallel [120]$, parallel to the edge of the hexagonal crystal, yields a similar result with a slightly larger Curie constant: $C = 0.498(8)$ emu/mol Cu K ($\mu_{\text{eff}} = 1.99 \mu_B$), $\Theta = 43(2)$ K, and $\chi_0 = -3.0(1) \times 10^{-4}$ emu/mol Cu. Note that no clear anisotropy was observed in $\chi(T)$ in $\mathbf{H} \parallel [120]$ and $\mathbf{H} \parallel \mathbf{a}$ above 1.8 K. The linear behavior of the inverse susceptibility $(\chi - \chi_0)^{-1}$ justifies the fits [Fig. 2(a)]. The enhancement of μ_{eff} with respect to the spin-only value ($1.73 \mu_B$) is typical for Cu^{2+} compounds and shows a slight anisotropy in the g factor ($g_{\parallel} \simeq 2.24$ vs $g_{\perp} \simeq 2.30$).

Below ~ 50 K, the susceptibility starts to deviate from the Curie-Weiss behavior [Fig. 2(a)]. In accord with a previous study [20], neither anomalies indicative of magnetic ordering nor signatures of a spin gap formation were observed down to 1.8 K. To obtain more information on the low- T regime, we measured magnetization of the single-crystal samples down to 0.1 K by the capacitive Faraday method [24]. Again, the results do not show any sign of magnetic ordering, despite the relatively large Θ value [Fig. 2(b)]. This is one of the key experimental results. Furthermore, the low- T susceptibility is highly anisotropic and is significantly suppressed in $\mathbf{H} \parallel [120]$ compared to that in $\mathbf{H} \parallel \mathbf{c}$. More importantly, at the lowest field measured (0.1 T), χ_{\parallel} exhibits paramagnetic behavior ($\chi_{\parallel} \propto 1/T$) down to 0.1 K, whereas χ_{\perp} appears to saturate at low T . So the longitudinal and transverse responses are *qualitatively* different. This is another key experimental result, which suggests the presence of anisotropic interactions.

High-field magnetization measurements. In a magnetic field, the star lattice models can feature exotic behavior with a cascade of phases [11,13]. To study the emergence of field-induced phases in DiMACuS, we performed magnetization measurements in a pulsed high-magnetic field. Measurements at 4.2 K up to 65 T were performed by the induction method in a magnetic field with the pulse length of 4 ms [Fig. 2(c)]. As in the magnetic susceptibility, M is much larger in $\mathbf{H} \parallel \mathbf{c}$ than in $\mathbf{H} \parallel [120]$, with the powder data taking intermediate values. While the magnetization increases rapidly below 20 T, its slope $\frac{\partial M}{\partial H}$ first decreases as the field increases, but then saturates around 30 T, which is reminiscent of a magnetization plateau.

This feature is examined in more detail by measuring the magnetization process at 0.13 K [Fig. 2(d)]. In $\mathbf{H} \parallel \mathbf{c}$, the magnetization increases steeply and becomes essentially flat above 2.5 T (with $\frac{\partial M}{\partial H}$ exhibiting a saturating behavior already at 1 T), at around $0.37 \mu_B/\text{Cu}$. With $g_{\parallel} \simeq 2.24$ (estimated

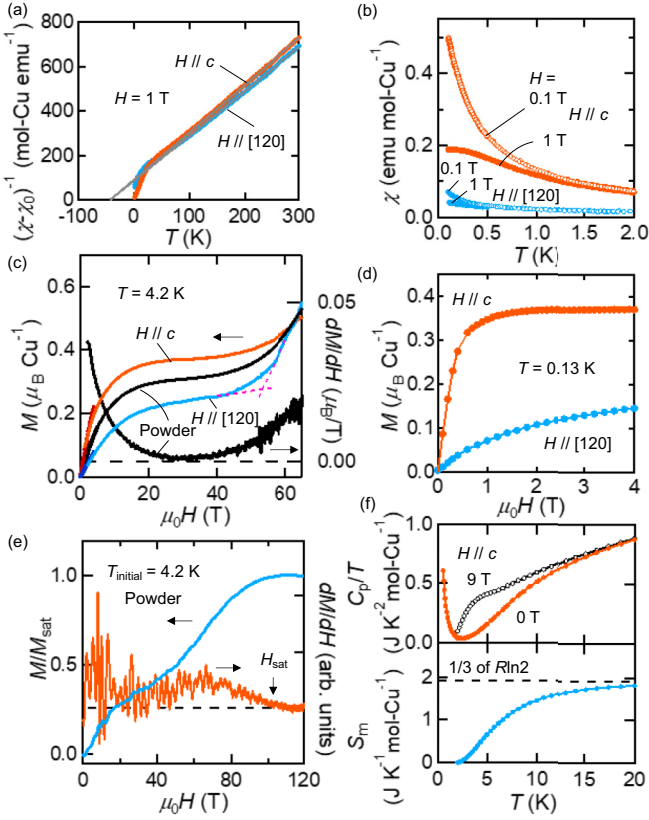


FIG. 2. (a) T dependence of inverse susceptibility at 1 T and the Curie-Weiss fits. (b) Magnetic susceptibility at 0.1 and 1 T below 2 K. (c) Magnetization curves of the single crystal and powder sample at 4.2 K and up to 65 T. The magnetic field derivative for powder data is also shown. (d) Magnetization curve of the single crystal at 0.13 K. (e) Magnetization curve of the powder sample up to 120 T measured at $T_{\text{initial}} = 4.2$ K and its field derivative. (f) Specific heat divided by T at 0 and 9 T below 20 K and magnetic entropy estimated as in the main text.

from the Curie-Weiss fit), this is close to $1/3$ of the full moment. Therefore, we conclude that DiMACuS exhibits a $1/3$ magnetization plateau in $\mathbf{H} \parallel \mathbf{c}$. On the other hand, the magnetization in $\mathbf{H} \parallel [120]$ gradually increases without a clear flat region. The presence of a clear $1/3$ plateau for $\mathbf{H} \parallel \mathbf{c}$ despite the presence of anisotropic interactions is the third key experimental result.

The end of the plateau-like regime is signaled by the increase of $\frac{\partial M}{\partial H}$ which becomes noticeable around 40 T at 4.2 K. A more evident increase of magnetization is observed in $\mathbf{H} \parallel [120]$, where magnetization is suppressed at low magnetic fields. The extrapolated (dashed) lines [Fig. 2(c)] cross at 53 T, which may be considered as the onset of the jump to saturation for $\mathbf{H} \perp \mathbf{c}$. To study the behavior in higher fields, we performed magnetization measurements by the induction method up to around 120 T [Fig. 2(e)] generated by the destructive single turn coil method with a pulse length of $7 \mu\text{s}$ [25]. The powder sample was used due to the small sample space. $\frac{\partial M}{\partial H}$ exhibits a minimum at around 30 T and a maximum at around 65 T, which are consistent with the data obtained in the measurements up to 65 T, albeit with large noise caused by

the magnetic field generation. The field derivative becomes small and almost constant above 105 T, indicating that the fully polarized state is reached. Indeed, the magnetization at 105 T is approximately three times larger than the value at 30 T in the $1/3$ plateau-like region.

Specific heat measurements. The specific heat C_p of the single crystal was measured by the relaxation method using a commercial apparatus (PPMS, Quantum Design). At zero field, C_p/T shows a low- T upturn [Fig. 2(f)], which may indicate long-range ordering below 0.1 K (the lowest T in χ measurements). Measurements in 9 T applied along the c axis reveal a considerable enhancement of C_p/T above 2 K. While we do not have data below 2 K at 9 T, the system is already in the $1/3$ plateau phase [Fig. 2(d)], and the remaining magnetic entropy should be small. Hence, the field-induced enhancement of C_p/T above 2 K gives strong evidence for the existence of low-lying magnetic excitations residing below 2 K in zero field and which are propelled to higher energies by the field. This behavior is a hallmark of isolated or weakly interacting spin- S degrees of freedom emerging at low-energy scales. To shed further light on this, we estimate the entropy content of the low-lying excitations by integrating the difference of C_p/T between 9 and 0 T from 2 K up to 20 K. The obtained entropy is approximately 1.8 J/K mol Cu at 20 K, very close to $\frac{1}{3}R \ln 2$. This value is associated with *one* doublet degree of freedom per Cu triangle. This is the fourth key experimental finding.

Microscopic modeling. We now set out to develop a microscopic description that accounts for all experimental findings. Based on the crystal structure of DiMACuS, we can identify three inequivalent exchange paths between neighboring spins, J_T , J_D , and J_H [Fig. 1(b)], which can be estimated by first-principles density-functional-theory (DFT) calculations. To this end, we employed the generalized gradient approximation (GGA) [26] as implemented in the full-potential code FPLO version 21 [27]. Following Ref. [20], we keep only $\text{Cu}_3(\text{OH})(\text{SO}_4)_4$ magnetic layers and discard the organic cations. A uniform background charge was used to retain electroneutrality. Since the experimental structure features the unusually short hydroxyl bond length of about 0.82 \AA , we calculated the optimal hydrogen position ($z/c = 0.370053$) with respect to the GGA total energy. Next, we performed magnetic supercell calculations using the GGA + U functional with the Coulomb repulsion U_d of $8.5 \pm 1 \text{ eV}$ and the Hund's exchange J_d of 1 eV, respectively, and the fully localized limit as the double counting correction. Magnetic exchange integrals were estimated by mapping the GGA + U energies of eight different magnetic configurations onto a classical Heisenberg model; the resulting redundant linear problem was solved by the least-squares method. For $U_d = 9.5 \text{ eV}$, we found $J_T = 81.5 \text{ K}$, $J_D = 5.4 \text{ K}$, and $J_H = 0.3 \text{ K}$ (practically negligible) [28]. This choice of U_d is justified by the excellent agreement between the calculated Weiss temperature $\Theta = \frac{1}{2}J_T + \frac{1}{4}J_D + \frac{1}{2}J_H = 42.2 \text{ K}$ and its experimental value.

The J_T - J_D model in the strong-coupling limit $J_T \gg J_D$ suggests an effective description in terms of isolated $S = 1/2$ Heisenberg triangles. Indeed, the isolated triangle model with $J_T = 58.5 \text{ K}$ and $g = 2.205$ accounts for the experimental $\chi(T)$ measured in $\mathbf{H} \parallel \mathbf{c}$ [28] and reproduces the $1/3$ plateau, which corresponds to each triangle being in the $S_z = \frac{1}{2}$ member

of the Zeeman-split doublet (a similar situation is observed in the frustrated cuprate volborthite featuring magnetic trimers [29,30]).

However, the isotropic model fails to describe the observed anisotropy. Moreover, an isolated $S = 1/2$ AFM Heisenberg triangle has two doublet GSs and not one [28], and therefore does not capture the $\frac{1}{3}R \ln 2$ entropy content of the low-lying excitations deduced from the C_p data. To determine the relevant anisotropies, we performed full relativistic noncollinear DFT + U total energy calculations and computed the bilinear exchange matrix $J_T^{\alpha\beta}$ using the energy-mapping method [31]. Total energies were calculated with the projector-augmented wave code VASP version 5.4.4 [32] using standard pseudopotentials [33] and an energy cutoff of 400 eV. These calculations were done on $2 \times 2 \times 2$ k -mesh; for the interaction parameters, we used U_d and J_d of 9.5 and 1 eV, respectively. In this way, we found that [28] (i) the symmetric and traceless part of the exchange anisotropy is extremely weak and can be safely disregarded, and (ii) the dominant Heisenberg exchange in DiMACuS is accompanied by a sizable DM anisotropy on the J_T bonds (the DM anisotropy on the J_D bonds vanishes due to inversion symmetry). The \mathbf{D}_T vectors are perpendicular to the respective bonds and form acute angles of $\sim 50^\circ$ to each other, with $D_T^\parallel/J_T = 0.274$, $D_T^\perp/J_T = 0.493$, and $|\mathbf{D}_T|/J_T = 0.56$ [28]. The latter ratio is remarkably large, yet not unprecedented for cuprates [34,35]. The sizable DM interaction is supported by the simulated susceptibility showing excellent agreement for both field directions down to ~ 10 K [Fig. 3(a)]. It allows us to further refine the magnetic exchanges: $J_T = 57$ K and $|\mathbf{D}_T|/J_T = 0.42$.

The DM interactions have a drastic impact on the physics of weakly coupled triangles. The leading contribution stems from D_T^\parallel , while the influence of in-plane DM components is zero to first order in D_T^\perp/J_T [28]. Our numerical simulations (Fig. 3 and Ref. [28]), which include all DM components, confirm this explicitly. So, to a good approximation, D_T^\perp can be safely disregarded, and the system effectively features two emergent (i.e., approximate) symmetries at low energies: U(1) spin rotation and a threefold spatial rotation, both around the \mathbf{c} axis.

Hence, for $\mathbf{H} \parallel \mathbf{c}$, the states of the system have well-defined total moment S_z along \mathbf{c} and chirality ℓ (irreps of threefold spatial rotation). Now, in the absence of D_T^\parallel , each triangle has two doublet GSs, separated by the $S = 3/2$ quartet by a gap of $3J_T/2 \simeq 85$ K [Fig. 3(b), left]. At lower temperatures, the J_T scale disappears from the problem, and we are left with two doublets of opposite chirality ℓ . D_T^\parallel lifts the degeneracy of the two doublets and introduces a new energy scale, the gap $\Delta = \sqrt{3}|D_T^\parallel| \simeq 35$ K [Fig. 3(b), right]. At lower T , this scale also disappears from the problem, and we are left with one doublet per triangle, in agreement with the C_p data [see Fig. 3(d), which also demonstrates the characteristic field-induced entropic shift seen experimentally, at the level of two coupled triangles].

The peculiar anisotropy of DiMACuS is governed by the emergent U(1) symmetry: unaffected by a field along \mathbf{c} , but broken for fields perpendicular to \mathbf{c} . This is manifest as follows [28]. D_T^\parallel gives rise to a characteristic locking between S_z

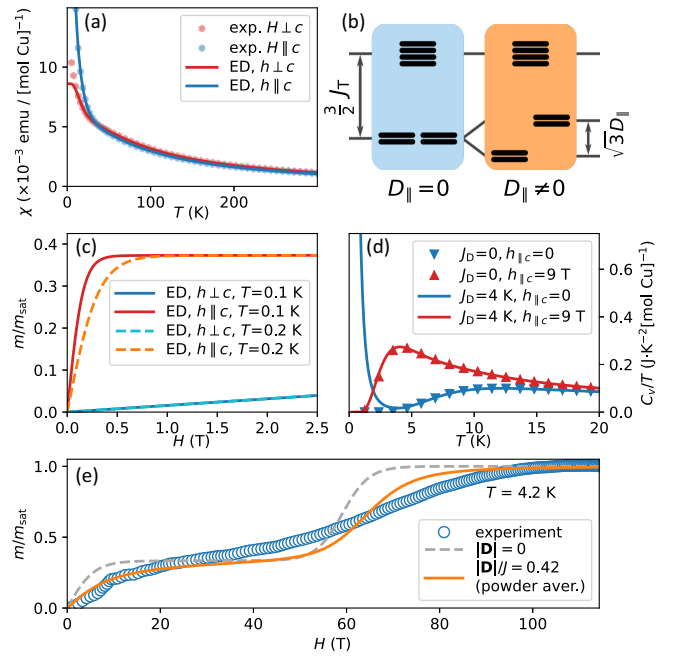


FIG. 3. (a) Magnetic susceptibility at 1 T for different field directions (symbols) and fits (lines) with the anisotropic triangle Heisenberg model with $|\mathbf{D}|/J = 0.42$ ($J = 56.5$ K, $g = 2.249$, and $\chi_0 = -2.82 \times 10^{-4}$ emu/mol Cu for $\mathbf{H} \perp \mathbf{c}$ and $J = 58.5$ K, $g = 2.205$, and $\chi_0 = -3.18 \times 10^{-4}$ emu/mol Cu for $\mathbf{H} \parallel \mathbf{c}$). (b) Spectra of a Heisenberg triangle and a triangle with D_T^\parallel . (c) Magnetization curve simulated for the parameters from panel (a). (d) Simulated specific heat for an isolated triangle ($J_D = 0$) at 0 and 9 T, and for two triangles coupled with $J_D = 4$ K. (e) Powder-averaged magnetization isotherm of an isolated triangle with $|\mathbf{D}|/J = 0.42$ (solid line, obtained by averaging over a Fibonacci sphere of 500 points), in comparison with the isotropic triangle (dashed lines) and the experiment (circles). MATPLOTLIB [36] was used for plotting panels (a) and (c)–(e). For plotting scripts and numerical data, see Ref. [37].

and ℓ : the $S_z = \pm 1/2$ members of one doublet have $\ell = \pm 1$, whereas for the other doublet $\ell = \mp 1$. Hence, a field along \mathbf{c} does not couple the two doublets; instead, it gives rise to a Zeeman splitting for each doublet, the Curie-like susceptibility $\chi_\parallel \propto 1/(4T)$ at temperatures sufficiently below Δ , and the flat $1/3$ magnetization plateau [Fig. 3(c)], independent of D_T^\parallel . By contrast, an in-plane field breaks the U(1) symmetry explicitly and thus couples the two doublets, leading to a standard level repulsion, with each doublet retaining its twofold degeneracy. At low- T , χ_\perp approaches a finite value [Fig. 3(a)], inversely proportional to D_T^\parallel , and the magnetization behaves as $h/\sqrt{h^2 + 3(D_T^\parallel)^2}$ (where $h = g_\perp \mu_B H$): linear at low fields [Fig. 3(c)], and asymptotically approaching the $1/3$ value, without developing a flat plateau. Precisely this behavior is observed experimentally in Figs. 2(c) and 2(d).

Next, we consider the high-field magnetization of the isolated-triangle model. On exiting the $1/3$ plateau, the magnetization shows an almost abrupt jump to full saturation at H^* equal to $3/2J_T$ in the isotropic case. D_T propels the saturation to higher fields, but only for $\mathbf{H} \parallel \mathbf{c}$. By using the above refined values of J_T and D_T in analytical expressions for H^* [28], we obtain $H_\parallel^* \simeq 64$ T and $H_\perp^* \simeq 56$ T. The latter is

in satisfactory agreement with the endpoint of the plateau-like region for $\mathbf{H} \perp \mathbf{c}$ [Fig. 2(c)]. The difference between H_{\parallel}^* and H_{\perp}^* is further corroborated by numerical simulations of the powder-averaged magnetization [Fig. 3(e)]. We note finally that, in the powder measurements, the value of H^* is distributed between H_{\parallel}^* and H_{\perp}^* , effectively destroying the magnetization jumps predicted for both field directions.

The isolated triangle model does not fully account for the specific heat data: the expected gapped zero-field spectrum [Fig. 3(d)] is in sharp contrast with the divergence observed below 0.5 K [Fig. 2(f)]. The root cause of this discrepancy is interactions between the triangles: for a minimal model of two triangles coupled with J_D , such a peak readily appears at a temperature very close to the experimentally observed [Fig. 3(d)]. Obviously, the actual connectivity of triangles in DiMACuS follows a honeycomb lattice, and its realistic simulation requires a much larger number of spins. The interactions between the triangles can be described by an effective model, in which each spin triangle is treated as a rigid entity. While a full analysis of this model is beyond our scope, we note that the rescaling of effective spin lengths also reduces the dominant exchange scale from J_D to $J_D/9$, which may explain the lack of ordering down to 0.1 K.

Finally, we comment on the slight orientational disorder in the dimethylammonium molecule and the defect in the crystal water intercalated between the magnetic layers [20]. On the organic molecular Mott insulator, there is an argument that random freezing of the electric polarization of the molecules causes magnetic bond randomness, which can result in a gapless spin liquid behavior [38]. In contrast to the organic Mott insulator where the molecule itself carries the spin, the dimethylammonium and H_2O molecules in DiMACuS are nonmagnetic and not involved in the magnetism in the $\text{Cu}_3(\text{OH})(\text{SO}_4)_4$ layer. Indeed, no structural disorder is reported in the $\text{Cu}_3(\text{OH})(\text{SO}_4)_4$ layer [20]. While we anticipate the effects of disorder on the magnetism to be weak, this may still hinder the ordering at very low T .

Summary and outlook. We demonstrate DiMACuS as a realization of a spin- $\frac{1}{2}$ star lattice antiferromagnet, one of the paradigms for geometric frustration and resonating valence bond physics. The main experimental puzzles, including the absence of magnetic ordering down to very low temperatures, the characteristic field-induced entropic shift seen in the specific heat data, and the peculiar anisotropy in the magnetic response, can all be accounted for by the strong frustration in the Cu triangles and the sizable Dzyaloshinskii-Moriya anisotropy. Further studies are needed to clarify if DiMACuS orders magnetically at a very low temperature and investigate the possible role of disorder.

Star lattice magnets are known to exhibit a chiral spin liquid state in the presence of Kitaev-type anisotropic interaction [15]. Substituting Cu with divalent Co may substantially enhance the exchange anisotropy and give rise to bond-dependent interactions that underlie the Kitaev physics. As demonstrated in a kagome system, cobaltate analogs of cuprates exist in nature [39] and can be synthesized [40]. Synthesis of relative materials with different magnetic cations will pave the way to explore the star lattice magnetism from the extreme quantum case to the classical large- S limit.

Acknowledgments. We thank Dr. D. Nishio-Hamane for taking the optical image of the crystal. We thank Professor Z. Hiroi for fruitful discussions and U. Nitzsche for technical assistance. H.I. was supported by JSPS KAKENHI Grants No. JP22H04467 and No. JP22K13996. Y.H.M. was supported by JSPS KAKENHI, Grant-in-Aid for Transformative Research Areas (A) No. 23H04860. Y.S. was supported by JSPS KAKENHI Grants No. 23H04870 and No. 23K03314. O.J. was supported by the Leibniz Association through the Leibniz Competition and the German Forschungsgemeinschaft (DFG, German Research Foundation) through SFB 1143 (Project ID 247310070). I.R. acknowledges the support by the Engineering and Physical Sciences Research Council, Grant No. EP/V038281/1.

-
- [1] C. Lacroix, P. Mendels, and F. Mila, *Introduction to Frustrated Magnetism: Materials, Experiments, Theory*, Springer Series in Solid-State Sciences (Springer, Berlin, 2011), Vol. 164.
- [2] J. Richter, J. Schulenburg, and A. Honecker, Quantum magnetism in two dimensions: from semi-classical Néel order to magnetic disorder, in *Lecture Notes in Physics*, edited by U. Schollwöck, J. Richter, D. Farnell, and R. Bishop (Springer, Berlin, 2004), Vol. 645, pp. 85–153.
- [3] P. W. Anderson, The resonating valence bond state in La_2CuO_4 and superconductivity, *Science* **235**, 1196 (1987).
- [4] A. Kitaev, Anyons in an exactly solved model and beyond, *Ann. Phys.* **321**, 2 (2006).
- [5] S. Yan, D. A. Huse, and S. R. White, Spin-liquid ground state of the $S = 1/2$ kagome Heisenberg antiferromagnet, *Science* **332**, 1173 (2011).
- [6] S. Depenbrock, I. P. McCulloch, and U. Schollwöck, Nature of the spin-liquid ground state of the $S = 1/2$ Heisenberg model on the kagome lattice, *Phys. Rev. Lett.* **109**, 067201 (2012).
- [7] R. R. P. Singh and D. A. Huse, Ground state of the spin- $1/2$ kagome-lattice Heisenberg antiferromagnet, *Phys. Rev. B* **76**, 180407(R) (2007).
- [8] S. Capponi, V. R. Chandra, A. Auerbach, and M. Weinstein, p6 chiral resonating valence bonds in the kagome antiferromagnet, *Phys. Rev. B* **87**, 161118(R) (2013).
- [9] A. Ralko, F. Mila, and I. Rousochatzakis, Microscopic theory of the nearest-neighbor valence bond sector of the spin- $\frac{1}{2}$ kagome antiferromagnet, *Phys. Rev. B* **97**, 104401 (2018).
- [10] D. J. J. Farnell, O. Götze, J. Richter, R. Bishop, and P. H. Y. Li, Quantum $s = 1/2$ antiferromagnets on Archimedean lattices: The route from semiclassical magnetic order to nonmagnetic quantum states, *Phys. Rev. B* **89**, 184407 (2014).
- [11] J. Richter, J. Schulenburg, A. Honecker, and D. Schmalfuß, Absence of magnetic order for the spin-half Heisenberg antiferromagnet on the star lattice, *Phys. Rev. B* **70**, 174454 (2004).
- [12] B.-J. Yang, A. Paramekanti, and Y. B. Kim, Competing quantum paramagnetic ground states of the Heisenberg antiferromagnet on the star lattice, *Phys. Rev. B* **81**, 134418 (2010).

- [13] S.-J. Ran, W. Li, S.-S. Gong, A. Weichselbaum, J. von Delft, and G. Su, Emergent spin-1 trimerized valence bond crystal in the spin-1/2 Heisenberg model on the star lattice, *Phys. Rev. B* **97**, 075146 (2018).
- [14] S. S. Jahromi and R. Orús, Spin-1/2 Heisenberg antiferromagnet on the star lattice: Competing valence-bond-solid phases studied by means of tensor networks, *Phys. Rev. B* **98**, 155108 (2018).
- [15] H. Yao and S. A. Kivelson, Exact chiral spin liquid with non-Abelian anyons, *Phys. Rev. Lett.* **99**, 247203 (2007).
- [16] M. G. Townsend, G. Longworth, and E. Roudaut, Triangular-spin, kagome plane in jarosites, *Phys. Rev. B* **33**, 4919 (1986).
- [17] H. Ishikawa, Y. Okamoto, and Z. Hiroi, Magnetic properties of the spin-1/2 deformed kagome antiferromagnet edwardsite, *J. Phys. Soc. Jpn.* **82**, 063710 (2013).
- [18] S. K. Pati and C. N. R. Rao, Kagome network compounds and their novel magnetic properties, *Chem. Commun.* 4683 (2008).
- [19] A. V. Powell, P. Leyva-Bailen, P. Vaqueiro, and R. D. Sanchez, $\text{Co}_3(\text{SO}_4)_3(\text{OH})_2[\text{enH}_2]$: A new $S = 3/2$ kagome-type layered sulfate with a unique connectivity, *Chem. Mater.* **21**, 4102 (2009).
- [20] M. Sorolla, X. Wang, H.-J. Koo, M.-H. Whangbo, and A. J. Jacobson, Synthesis of the elusive $S = 1/2$ star structure: A possible quantum spin liquid candidate, *J. Am. Chem. Soc.* **142**, 5013 (2020).
- [21] H. Ishikawa, T. Okubo, Y. Okamoto, and Z. Hiroi, Kagome-triangular lattice antiferromagnet $\text{NaBa}_2\text{Mn}_3\text{F}_{11}$, *J. Phys. Soc. Jpn.* **83**, 043703 (2014).
- [22] K. Momma and F. Izumi, VESTA 3 for three-dimensional visualization of crystal, volumetric and morphology data, *J. Appl. Crystallogr.* **44**, 1272 (2011).
- [23] J. Rodríguez-Carvajal, Recent advances in magnetic structure determination by neutron powder diffraction, *Phys. B: Condens. Matter* **192**, 55 (1993).
- [24] Y. Shimizu, Y. Kono, T. Sugiyama, S. Kittaka, Y. Shimura, A. Miyake, D. Aoki, and T. Sakakibara, Development of high-resolution capacitive Faraday magnetometers for sub-Kelvin region, *Rev. Sci. Instrum.* **92**, 123908 (2021).
- [25] S. Takeyama, R. Sakakura, Y. H. Matsuda, A. Miyata, and M. Tokunaga, Precise magnetization measurements by parallel self-compensated induction coils in a vertical single-turn coil up to 103 T, *J. Phys. Soc. Jpn.* **81**, 014702 (2012).
- [26] J. P. Perdew, K. Burke, and M. Ernzerhof, Generalized gradient approximation made simple, *Phys. Rev. Lett.* **77**, 3865 (1996).
- [27] K. Koepnick and H. Eschrig, Full-potential nonorthogonal local-orbital minimum-basis band-structure scheme, *Phys. Rev. B* **59**, 1743 (1999).
- [28] See Supplemental Material at <http://link.aps.org/supplemental/10.1103/PhysRevB.109.L180401> for (i) details of the first-principles calculations of microscopic interactions, (ii) the quantum-mechanical problem of a single spin-1/2 triangle with DM interactions, and (iii) simulations of the magnetic susceptibility of this model and fits to the experimental $\chi(T)$ of DiMACuS.
- [29] H. Ishikawa, M. Yoshida, K. Nawa, M. Jeong, S. Krämer, M. Horvatić, C. Berthier, M. Takigawa, M. Akaki, A. Miyake *et al.*, One-third magnetization plateau with a preceding novel phase in volborthite, *Phys. Rev. Lett.* **114**, 227202 (2015).
- [30] O. Janson, S. Furukawa, T. Momoi, P. Sindzingre, J. Richter, and K. Held, Magnetic behavior of volborthite $\text{Cu}_3\text{V}_2\text{O}_7(\text{OH})_2 \cdot 2\text{H}_2\text{O}$ determined by coupled trimers rather than frustrated chains, *Phys. Rev. Lett.* **117**, 037206 (2016).
- [31] H. Xiang, C. Lee, H.-J. Koo, X. Gong, and M.-H. Whangbo, Magnetic properties and energy-mapping analysis, *Dalton Trans.* **42**, 823 (2013).
- [32] G. Kresse and J. Furthmüller, Efficient iterative schemes for *ab initio* total-energy calculations using a plane-wave basis set, *Phys. Rev. B* **54**, 11169 (1996); Efficiency of *ab-initio* total energy calculations for metals and semiconductors using a plane-wave basis set, *Comput. Mater. Sci.* **6**, 15 (1996).
- [33] G. Kresse and D. Joubert, From ultrasoft pseudopotentials to the projector augmented-wave method, *Phys. Rev. B* **59**, 1758 (1999).
- [34] O. Janson, I. Rousochatzakis, A. A. Tsirlin, M. Belesi, A. A. Leonov, U. K. Röbller, J. van den Brink, and H. Rosner, The quantum origins of skyrmions and half-skyrmions in Cu_2OSeO_3 , *Nat. Commun.* **5**, 5376 (2014).
- [35] A. Panther, A. A. Tsirlin, and I. Rousochatzakis, Frustration relief and reorientation transition in the kagomelike dolerophanite Cu_2OSO_4 , *Phys. Rev. B* **108**, 224410 (2023).
- [36] J. D. Hunter, Matplotlib: A 2D graphics environment, *Comput. Sci. Eng.* **9**, 90 (2007).
- [37] Source code for generating Fig. 3 and ancillary numerical data can be accessed through a figshare repository at doi.org/10.6084/m9.figshare.24504163.
- [38] K. Watanabe, H. Kawamura, H. Nakano, and T. Sakai, Quantum spin-liquid behavior in the spin-1/2 random Heisenberg antiferromagnet on the triangular lattice, *J. Phys. Soc. Jpn.* **83**, 034714 (2014).
- [39] A. V. Kasatkin, J. Plasil, I. V. Pekov, D. I. Belakovskiy, F. Nestola, J. Cejka, M. F. Vidasina, F. Zorzi, and B. Thorne, Karpenkoite, $\text{Co}_3(\text{V}_2\text{O}_7)(\text{OH})_2 \cdot 2\text{H}_2\text{O}$, a cobalt analogue of martyrite from the Little Eva mine, Grand County, Utah, USA, *J. Geosci.* **60**, 251 (2015).
- [40] Y. Haraguchi, T. Ohnoda, A. Matsuo, K. Kindo, and H. A. Katori, Perfect kagome-lattice antiferromagnets with $J_{\text{eff}} = 1/2$: The Co^{2+} analogs of the copper minerals volborthite and vesignieite, *Phys. Rev. B* **106**, 214421 (2022).